DOI: https://doi.org/10.68732/cd8fc2e65a999f46

ISBN: 978-9989-2053-6-1

Numerical modelling of cracking in granite due to Joule heating and piezoelectric actuation

T. Saksala
Tampere University, Tampere, Finland
timo.saksala@tuni.fi

Abstract

Traditional comminution and drilling of hard rock, being based on mechanical breakage, suffers from severe tool wear. This has spurred intensive search for advanced preconditioning methods to facilitate mechanical breakage. One of these method uses high voltage electric pulses to fracture rock. This can happen directly, via Joule heating, whereby a rapid rise of the pressure and temperature in the electric breakdown channel between electrodes break the rock. Alternatively, the quartz phase in quartz-bearing rocks can be actuated by the converse piezoelectric effect.

In the present study, a numerical model to simulate both techniques, the Joule heating and the piezoelectric actuation of the quartz phase, is developed. This task involves developing a rock fracture model and a solution scheme for the underlying coupled piezoelectro-thermo-mechanical problem. As to the rock fracture model, the embedded discontinuity finite elements approach is chosen. In this approach, a crack with the normal parallel to the first principal direction is introduced into a finite element upon violation of the Rankine criterion. Moreover, random clusters of finite elements representing the constituent minerals with their respective mechanical, thermal and electrical properties describe the rock heterogeneity. A staggered approach, with explicit time marching for the mechanical equation of motion, is applied in solving the coupled system of equations at the global level.

In the numerical examples, cracking of a heterogeneous granitic rock specimen under high voltage boundary condition is simulated in axisymmetric conditions. The results demonstrate that at lower voltages cracking is mainly due to Joule heating while at higher level, ~2.5 kV, cracks are induced also by the piezoelectric effect. Such a modelling technique is an asset that facilitates geotechnical project risk management by allowing numerical investigation of different physical and operational factors influencing the electro-pulse based preconditioning of rock mass.

Keywords

Piezoelectric actuation, Joule heating, rock fracture, numerical modelling, finite elements.

1 Introduction

Traditional drilling and mining operations are based on mechanical breakage, e.g. by percussion and rotary drilling methods. However, there techniques incur high costs via tool wear and low penetration in hard, say granitic, formations. These deficiencies have spurred intensive research for non-conventional drilling methods where a non-mechanical agent, such as thermal jet (Rossi et al. 2018) or high-voltage electric pulse (Liu et al. 2023) assists or totally replaces the mechanical breakage action. Despite considerable advances, these methods are still at the research and development stage. The present study attempts to contribute to this research by a numerical study.

The method exploiting high voltage electric pulses is based on the electrical breakdown phenomenon of the material via rapid increase of pressure and temperature in the breakdown (plasma) channel, leading to spalling of the rock surface. When the applied voltage is high enough, cracking may happen in granite via the converse piezoelectric effect in quartz mineral (Saksala et al. 2020). In the present study, these two phenomena are numerically studied. More precisely, a numerical code is developed to simulate these phenomena, i.e. Joule heating and the converse piezoelectric effect in numerical granitic rock. As the present study is of theoretical-speculative nature, no experimental validation is provided at this preliminary stage of research.

2 Rock Fracture Model

Rock fracture is described by the embedded discontinuity finite element approach (Saksala et al. 2015). Accordingly, if the stress in a finite element exceeds the first principal stress, a displacement discontinuity (crack) with the normal parallel to the first principal direction is embedded in that element. Then, for a 3-node triangle element with a discontinuity, the displacement and strain fields are written as

$$\mathbf{u}(\mathbf{x}) = N_i(\mathbf{x})\mathbf{u}_i^e + M_{\Gamma_d}(\mathbf{x})\boldsymbol{\alpha}_d \text{with } M_{\Gamma_d}(\mathbf{x}) = H_{\Gamma_d}(\mathbf{x}) - \varphi(\mathbf{x}) \tag{1}$$

$$\boldsymbol{\varepsilon}(\mathbf{x}) = (\nabla N_i \otimes \mathbf{u}_i^e)^{sym} - (\nabla\varphi(\mathbf{x}) \otimes \boldsymbol{\alpha}_d)^{sym} + \delta_{\Gamma_d}(\mathbf{n} \otimes \boldsymbol{\alpha}_d)^{sym} \tag{2}$$

where N_i and $\mathbf{u}_i^e$ are the standard interpolation functions and nodal displacements (i = 1,2,3 with summation on repeated indices), respectively, and the displacement jump is denoted by $\boldsymbol{\alpha}_d$. Moreover, H_{Γ_d} and δ_{Γ_d} are the Heaviside function and its gradient, the Dirac delta function at a discontinuity. Furthermore, the usual assumption with low order elements that $\nabla\boldsymbol{\alpha}_d \equiv \mathbf{0}$ was made in arriving atEq. (2). This displacement jump is thus elementwise constant, similarly to the ordinary strain for a CST element.

The task of function M_{Γ_d}in (1) is to restrict the effect of $\boldsymbol{\alpha}_d$ inside the corresponding finite element, facilitating the handling of the essential boundary conditions. Function φ appearing in M_{Γ_d} is chosen so that its gradient is as parallel as possible to the crack normal $\mathbf{n}_d$ by the following criterion: $\varphi = \arg\max_{k=1,2}\left|\sum_{i=1}^{k}\nabla N_i \cdot \mathbf{n}_d\right| / \left\|\sum_{i=1}^{k}\nabla N_i\right\|$. The traction vector in the present approach is calculated by the Cauchy expression defining also the stress-strain relation

$$\mathbf{t}_{\Gamma_d} = \boldsymbol{\sigma} \cdot \mathbf{n}_d = \left(\mathbf{C}_\mathrm{e} : (\hat{\boldsymbol{\varepsilon}} - (\nabla\varphi(\mathbf{x}) \otimes \boldsymbol{\alpha}_d)^{sym}) - \boldsymbol{\varepsilon}_\mathrm{pe} - \boldsymbol{\varepsilon}_\theta\right) \cdot \mathbf{n}_d \tag{3}$$

where$\mathbf{C}_\mathrm{e}$ is the elasticity tensor, $\hat{\boldsymbol{\varepsilon}} = (\nabla N_i \otimes \mathbf{u}_i^e)^{sym}$, and $\boldsymbol{\varepsilon}_\mathrm{pe} = \mathbf{d} \cdot \mathbf{E}$ is the piezoelectric strain with $\mathbf{d}$ and $\mathbf{E}$ being, respectively, the piezoelectric constants tensor and the electric field vector. Moreover, $\boldsymbol{\varepsilon}_\theta = \alpha\Delta\theta\mathbf{I}$ is the thermal strain, with $\alpha, \Delta\theta, \mathbf{I}$ being the thermal expansion coefficient, temperature increment and the second order identity tensor, respectively.

Next, a model for solving the crack opening vector and updating the relevant variables as well as the traction vector is needed. For this end, a computational plasticity inspired model presented by Saksala et al. (2015) is employed. The relevant model components, i.e. the loading functions, softening rules and evolution laws are defined as

$$\begin{aligned} \phi_\mathrm{t}\left(\mathbf{t}_{\Gamma_d}, \kappa, \dot{\kappa}\right) &= \mathbf{n}_d \cdot \mathbf{t}_{\Gamma_d} - \left(\sigma_\mathrm{t} + q(\kappa, \dot{\kappa})\right) \\ \phi_\mathrm{s}\left(\mathbf{t}_{\Gamma_d}, \kappa, \dot{\kappa}\right) &= \left|\mathbf{m}_d \cdot \mathbf{t}_{\Gamma_d}\right| - \left(\sigma_\mathrm{s} + \frac{\sigma_\mathrm{s}}{\sigma_\mathrm{t}} q(\kappa, \dot{\kappa})\right) \\ q = h\kappa + s\dot{\kappa}, h &= -g\sigma_\mathrm{t}\exp(-g\kappa), \quad g = \frac{\sigma_\mathrm{t}}{G_\mathrm{Ic}} \end{aligned} \tag{4}$$

$$\dot{\mathbf{t}}_{\Gamma_d} = -\mathbf{C}\colon(\nabla\varphi(\mathbf{x}) \otimes \dot{\boldsymbol{\alpha}}_d)\cdot\mathbf{n}_d$$
$$\dot{\boldsymbol{\alpha}}_d = \dot{\boldsymbol{\alpha}}_{\mathrm{I}} + \dot{\boldsymbol{\alpha}}_{\mathrm{II}} = \dot{\lambda}_{\mathrm{t}}\frac{\partial\phi_{\mathrm{t}}}{\partial\mathbf{t}_{\Gamma_d}} + \dot{\lambda}_{\mathrm{s}}\frac{\partial\phi_{\mathrm{s}}}{\partial\mathbf{t}_{\Gamma_d}},\quad \dot{\kappa} = -\dot{\lambda}_{\mathrm{t}}\frac{\partial\phi_{\mathrm{t}}}{\partial q} - \dot{\lambda}_{\mathrm{s}}\frac{\partial\phi_{\mathrm{s}}}{\partial q}$$
$$\dot{\lambda}_i \geq 0,\ \ \phi_i \leq 0,\ \ \dot{\lambda}_i\phi_i = 0 \quad (i = \mathrm{t},\mathrm{s})$$

where $\mathbf{m}_d$ denotes the unit tangent of a discontinuity,$\kappa, \dot{\kappa}$are the internal variable and its rate related to the softening law for a discontinuity,and σ_{t} and $\sigma_{\mathrm{s}}$are the tensile and shear strength, respectively. Moreover, parameter h is the softening modulus of the exponential softening rule while parameter g controls the initial slope of the softening curve and is calibrated by the mode I fracture energy G_{Ic}. Moreover, the Koiter's rule for bi-surface plasticity is applied in Eq. (4) where the total displacement jump is a sum of the contributions from mode I and mode II increments, while $\dot{\lambda}_{\mathrm{t}}, \dot{\lambda}_{\mathrm{s}}$ are the corresponding crack opening and sliding increments. Furthermore, rate-sensitivity is accommodated by adding a constant viscosity term, with s being the viscosity modulus, to the stress-like internal parameter q. The final equations in Eq. (4) are the consistency conditions.

3 Coupled piezoelectro-thermo-mechanical problem

While the constitutive equation in Eq. (3) couples the mechanical, electrical and temperature fields at the material point level, system (global) level equations are needed to solve for the primary field variables, which are the displacement, $\mathbf{u}$, the electric potential, $\boldsymbol{\phi}$, and the temperature, $\boldsymbol{\theta}$. The finite element discretized version of these equations are

$$\begin{aligned}\mathbf{M}\ddot{\mathbf{u}}_t + \mathbf{f}_t^{\mathrm{int}}(\mathbf{u}_t, \dot{\mathbf{u}}_t, \boldsymbol{\theta}_t, \boldsymbol{\phi}_t) &= \mathbf{0}\\ \mathbf{K}_{\phi\mathrm{u}}\mathbf{u}_t + \mathbf{K}_{\phi}\boldsymbol{\phi}_t &= \mathbf{0}\\ \mathbf{C}_{\theta}\dot{\boldsymbol{\theta}}_t + \mathbf{K}_{\theta}\boldsymbol{\theta}_t &= \mathbf{f}_t^{\theta}\end{aligned} \tag{5}$$

where

$$\begin{aligned}\mathbf{f}_t^{\mathrm{int}} &= \mathbf{A}_{\mathrm{e}=1}^{\mathrm{N_e}}\int_{V_{\mathrm{e}}}\mathbf{B}_{\mathrm{u}}^{\mathrm{e,T}}\boldsymbol{\sigma}_{\mathrm{e}}(\mathbf{u}_t, \dot{\mathbf{u}}_t, \boldsymbol{\theta}_t, \boldsymbol{\phi}_t)\mathrm{d}V,\quad \mathbf{M} = \mathbf{A}_{\mathrm{e}=1}^{\mathrm{N_e}}\int_{V_{\mathrm{e}}}\rho\mathbf{N}_{\mathrm{e}}{}^{\mathrm{T}}\mathbf{N}_{\mathrm{e}}\,\mathrm{d}V\\ \mathbf{C}_{\theta} &= \mathbf{A}_{\mathrm{e}=1}^{\mathrm{N_e}}\int_{V_{\mathrm{e}}}\rho c\mathbf{N}_{\theta}^{\mathrm{e,T}}\mathbf{N}_{\theta}^{\mathrm{e}}\mathrm{d}V,\quad \mathbf{K}_{\theta} = \mathbf{A}_{\mathrm{e}=1}^{\mathrm{N_e}}\int_{V_{\mathrm{e}}}k\mathbf{B}_{\theta}^{\mathrm{e,T}}\mathbf{B}_{\theta}^{\mathrm{e}}\mathrm{d}V\\ \mathbf{K}_{\mathrm{u}\phi} &= \mathbf{A}_{\mathrm{e}=1}^{\mathrm{N_e}}\int_{V_{\mathrm{e}}}\mathbf{B}_{\mathrm{u}}^{\mathrm{e,T}}\mathbf{e}\mathbf{B}_{\phi}^{\mathrm{e}}\mathrm{d}V,\qquad \mathbf{K}_{\phi\mathrm{u}} = \mathbf{K}_{\mathrm{u}\phi}{}^{\mathrm{T}},\qquad \mathbf{K}_{\phi} = \mathbf{A}_{\mathrm{e}=1}^{\mathrm{N_{el}}}\int_{V_{\mathrm{e}}}\mathbf{B}_{\phi}^{\mathrm{e,T}}\boldsymbol{\varepsilon}\mathbf{B}_{\phi}^{\mathrm{e}}\mathrm{d}V\\ \mathbf{f}_{\theta} &= \mathbf{A}_{\mathrm{e}=1}^{\mathrm{N_e}}\int_{V_{\mathrm{e}}}Q_j\mathbf{N}_{\theta}^{\mathrm{e,T}}\,\mathrm{d}V\end{aligned} \tag{6}$$

where the notations are: $\mathbf{A}$ is the finite element assembly operator; $\mathbf{B}_{\phi}^{\mathrm{e}}$ ($\mathbf{B}_{\theta}^{\mathrm{e}} = \mathbf{B}_{\phi}^{\mathrm{e}}, \mathbf{E} = \mathbf{B}_{\phi}^{\mathrm{e}}\boldsymbol{\phi}_e, \boldsymbol{\theta} = \mathbf{B}_{\theta}^{\mathrm{e}}\boldsymbol{\theta}_e$) is the gradient of the electric potential interpolation matrix $\mathbf{N}_{\phi}^{\mathrm{e}}$ ($\mathbf{N}_{\theta}^{\mathrm{e}} = \mathbf{N}_{\phi}^{\mathrm{e}}$), (analogously to $\mathbf{B}_{\mathrm{u}}^{\mathrm{e}}$ which is the gradient of displacement interpolation matrix $\mathbf{N}_{\mathrm{u}}^{\mathrm{e}}$); $\mathbf{M}$ is the mass matrix with ρ being the density;$\boldsymbol{\varepsilon}$ is the dielectric constant matrix; $\mathbf{e} = \mathbf{d}\mathbf{C}_{\mathrm{e}}$ is the piezoelectric coupling matrix; $\mathbf{C}_{\theta}$ is capacitance matrix with c being the heat capacity; $\mathbf{K}_{\theta}$ is the conductivity matrix with k being the thermal conductivity; $\mathbf{f}_{\mathrm{int}}$ is the internal force vector; $\mathbf{f}_{\theta}$ is the vector of thermal loading; $Q_j = \sigma_i\|\mathbf{E}\|^2$is the Joule (Ohmic) heating source (flux) with σ_i being the electric conductivity for each phase in rock.Equation system in Eq. (5) is solved in a staggered manner so that, first, the temperature field, $\boldsymbol{\theta}$, is solved by the explicit (forward) Euler scheme. Then, the mechanical response Eq. $(5)_1$ is explicitly advanced in time (also with the Euler scheme), and, finally, the electric potential, $\boldsymbol{\phi}$, is solved from the electrostatic balance equation Eq. $(5)_2$. Cracking affects the electrical properties so that the piezoelectric coupling term approaches zero as a crack in the quartz (being the only piezoelectric phase) opens, while the isotropic permittivity of all mineral phases approaches that of vacuum. Mathematically this is achieved by

$$\mathbf{e} = \exp(-g\|\boldsymbol{\alpha}_d\|)\mathbf{d}\mathbf{C}_{\mathrm{e}},\ \ \boldsymbol{\varepsilon} = \varepsilon_0(1 + \exp(-g\|\boldsymbol{\alpha}_d\|)(\varepsilon_r - 1))\mathbf{I} \tag{7}$$

whereε_r is the relative permittivity of the mineral, while g is as in Eq. (1), and $\|\boldsymbol{\alpha}_d\|$ is the norm of the crack opening vector.

It should be noted that material properties depend on temperature and deteriorate when the material undergoes damage by microcracking. However, these effects are ignored in this preliminary study, save the key property, i.e. the electric conductivity. As for the dielectric constant of granite as a bulk, it

is almost constant from room temperature to 1000 °C at 2450 MHz (Hartlieb et al. 2016). The electric conductivity for each (granitic) rock forming mineral is defined as (Walsh and Vogler 2020)

$$\sigma_{is} = A\exp(-B/k_b\theta) \tag{8}$$

where A and B are experimental constants, and k_b is the Boltzmann's constant (8.618E-5 eV/K).

When temperature is low, the rock conductivity is dominated by pore fluids. Here also, the work by Walsh and Vogler (2020) is followed by writing the Arps law for pores fluid conductivity under 150 °C as

$$\sigma_{if} = \sigma_{iref}\frac{\theta - 251.65}{\theta_{ref} - 251.65} \tag{9}$$

where σ_{iref} is the reference electrical conductivity at the reference temperature $\theta_{ref} = 150$ °C. At higher temperatures, the pore fluid conductivity is modelled by (Walsh and Vogler 2020)

$$\begin{aligned}\log_{10}\sigma_{if} &= -1.706 - 93.78/\theta + 0.8075\log_{10}c_{sw} + 3.0781\log_{10}\rho + \log_{10}\lambda_0 \\ \lambda_0 &= 1573 - 1212\rho + 537062/\theta - 208122721/\theta^2\end{aligned} \tag{10}$$

where $c_{sw} = 3$ wt% is the effective salinity of the pore water, and λ_0 is the molar conductivity of the brine. Finaly, the effect of pore fluid on the bulk conductivity is calculated by the Archie's law for two-component mixtures (Walsh and Vogler 2020):

$$\begin{aligned}\sigma_{ibulk} &= \sigma_{is}\left(1-\phi_f\right)^p + \sigma_{if}\phi_f^m \\ p &= \log_{10}(1-\phi_f^m)/\log_{10}(1-\phi_f)\end{aligned} \tag{11}$$

where ϕ_f is the fluid volume fraction within a mineral phase, and m= 1.5 is the Archie's exponent.

4 Numerical examples

4.1 Numerical rock model

Granite rock is modelled as an aggregate of random finite element clusters, which represent the rock forming mineral phases. The fraction of elements comprising each phase corresponds to the real mineral content in the rock. The feldspars plagioclase and K-feldspar are merged to a single feldspar phase. The finite element mesh and the spatially random mineral mesotructure with the potential (voltage) boundary condition are shown in Fig.1. The configuration with the cylindrical electrodes placed on the rock surface simulates drilling like conditions.

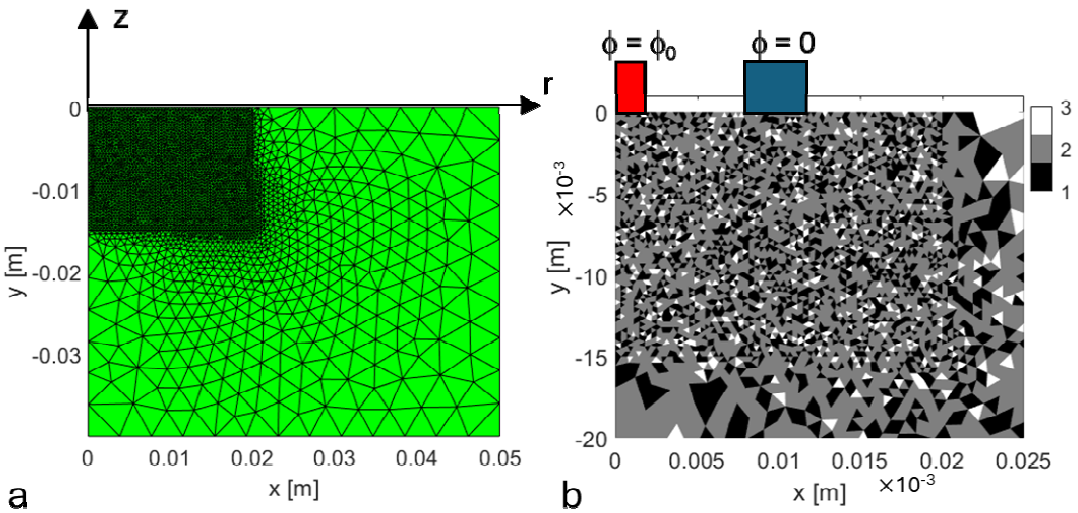


Fig. 1 Finite element mesh (6460 linear triangle elements) for axisymmetric simulations (a), and mineral mesostructure of the numerical rock with the voltage boundary conditions, i.e. the ground and positive electrodes (color code: 1 = quartz, 2 = feldspar, 3 = biotite) (b).

The material and model properties are given in Table 1 and 2.

Table 1.Material and model parameters for simulations I (Saksala et al. 2020, Hartlieb et al. 2016).

Mineral	f [%]	ρ[kg/m^3]	E [GPa]	ν	s [MPas/m]	σ_t [MPa]	σ_s [MPa]	G_{Ic} [J/m^2]	ε [F/m]
Quartz	30	2650	90	0.17	0.005	10	25	40	$4.5\varepsilon_0$
Feldspars	65	2620	60	0.29	0.005	8	25	40	$6.3\varepsilon_0$
Biotite	5	3050	60	0.20	0.005	7	25	28	$7.75\varepsilon_0$

ε_0= 8.854E-12F/m

Table 2 Material and model parameters for simulations II (Saksala et al. 2020, Hartlieb et al. 2016, Walsh and Vogler 2020).

Mineral	α [1/K]	c[J/kg·K]	k[W/m·K]	A [S/m]	B [eV]	ϕ_f [%]	d_r[m/V]	d_z [m/V]	d_{rz} [m/V]
Quartz	1.6E-5	730	4.94	544.57	0.82	0.9	–2.3E-12	2.3E-12	4.6E-12
Feldspars	0.75E-5	730	2.34	1.078	0.85	1.35	0	0	0
Biotite	1.21E-5	770	3.14	1.016E-6	0	0.9	0	0	0

The piezoelectric constants for quartz, i.e. d_r, d_z, d_{rz}, are given in local cylindrical coordinates. Thereby, the matrix including these coefficients in Eq. (3) needs to be rotated to the global coordinates. It is assumed that the quartz phase does not show any texture, i.e. systematic alignment of quartz crystal axes. Hence, the local constants are rotated to global ones by random Euler angles. In this case, the piezoelectric effect of a rock sample with quartz phase is at its weakest (Saksala 2021).

4.2 Rock sample under high voltage electric pulse

The problem described in Fig. 1 is now simulated setting the voltage $\phi_0 = 250$ kV. Fig. 2 and Fig. 3 show, respectively, the simulation results without and with the piezoelectric effect at t = 1 ms. In order to keep the computations stable, the electric conductivity (σ_{ibulk}) of an element is set to zero when the average temperature of the nodes of the element exceeds 1000 °C.

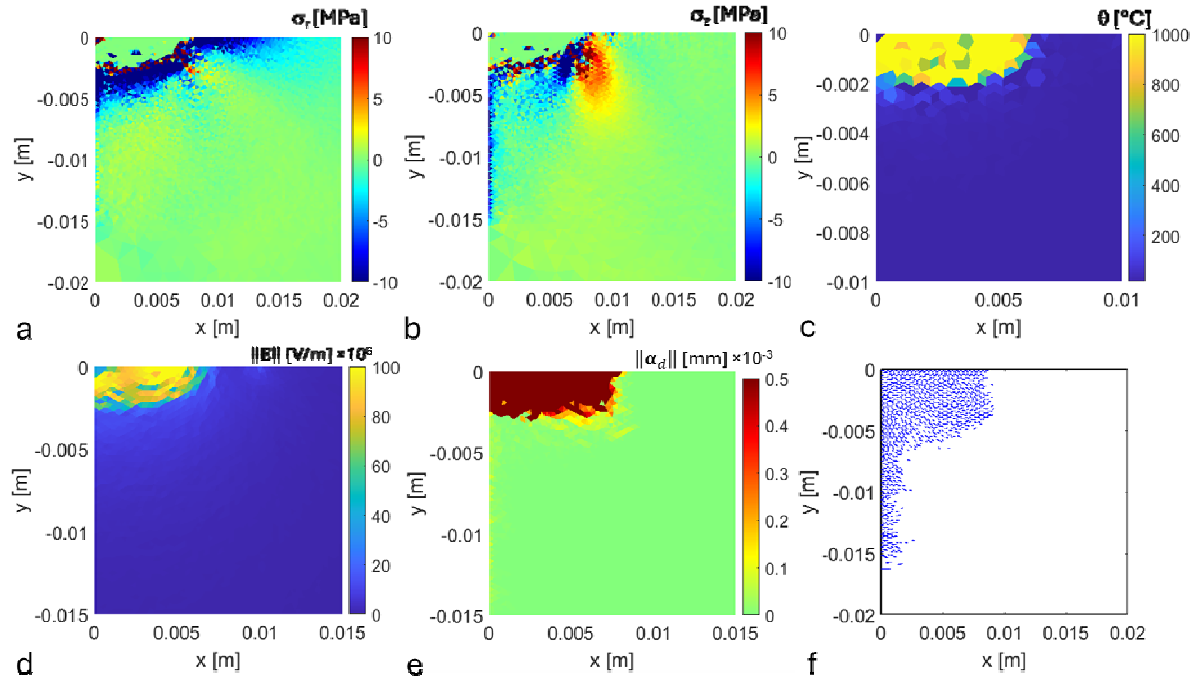


Fig. 2 Simulation results without piezoelectric effect: Radial stress (a); Stress in z-direction (b); Temperature field (c); Magnitude of electric field (d); Crack opening (e); Orientation of cracks (f).

Joule heating caused by the applied DC voltage results in significant temperature rise and consequent thermal stresses and cracking of the rock material, as attested in the results in Fig. 2. The excessive temperature rise, exceeding 1000 °C at which point the Joule heating source was set to zero, in the area between the electrodes, and the resulting crack opening, can be interpreted as crater formation. The stresses in this area are zero. The relevant simulation results with the piezoelectric effect are shown in Fig. 3.

The converse piezoelectric effect has a notable but not crucial influence on the high voltage induced cracking of granite rock. The shape of the cracked area differs from that produced when

piezoelectricity is disabled. However, the volume where crack opening is substantial is similar in both cases. Therefore, it seems the piezoelectricity can be ignored in modelling this problem.

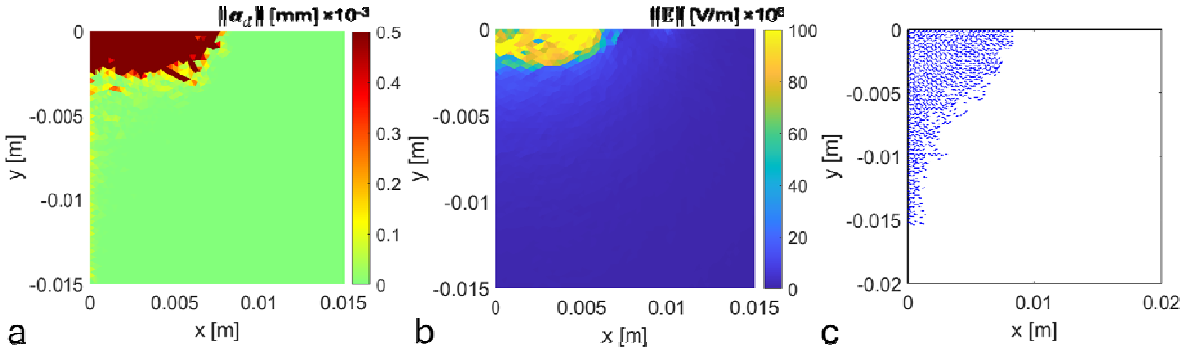


Fig. 3 Simulation results with piezoelectric effect: Crack opening(a); Magnitude of electric field (b); Orientation of cracks (c).

5 Conclusions

A finite element based computational procedure was developed to simulate cracking in granite rock due to high voltage direct current. The present model accounts for Joule heating and converse piezoelectric effect in the quartz phase. As the cracking is modelled explicitly with the embedded discontinuity finite element technology, the present method enables to study the crack orientation and opening magnitude. The numerical simulation mimicking drilling like boundary conditions revealed that the piezoelectric effect can be neglected and the Joule heating is the key phenomenon causing in cracking. In any case, the method predicts crater formation similar to that observed in experiments on electropulse drilling. It can be concluded that the present method could be used in research for the advanced drilling and comminution technologies based on preconditioning of rock before mechanical breakage. However, a full-blown 3D version should be developed for this end.

References

Rossi E, Kant MA, Borkeloh O, Saar MO, von Rohr PR (2018) Experiments on Rock-Bit Interaction during a Combined Thermo-Mechanical Drilling Method. PROCEEDINGS, 43rd Workshop on Geothermal Reservoir Engineering Stanford University, Stanford, California, February 12-14, 2018.

Liu W, Hu H, Zhu H (2023) The rock breaking mechanism of a combined high-voltage electric impulse-PDC bit drilling technology. Geothermics, 111:102723. https://doi.org/10.1016/j.geothermics.2023.102723

Saksala T, Moreno-Navarro P, Ibrahimbegovic A, Kane P-A (2020)Cracking of granite by actuation of piezoelectric properties of quartz by a high voltage electric charge: a numerical study. EUROCK2020, Trondheim, Norway, ISRM-EUROCK-2020-042 (Physical event not held due to COVID19 but the article is published at https://www.onepetro.org/conference-paper/ISRM-EUROCK-2020-042)

Saksala T, Brancherie B, Harari I, Ibrahimbegovic A (2015) Combined continuum damage-embedded discontinuity model for explicit dynamic fracture analyses of quasi-brittle materials. International Journalfor Numerical Methodsin Engineering, 101, 230–250.https://doi.org/10.1002/nme.4814

Walsh SDC, Vogler D (2020) Simulating electropulse fracture of granitic rock,International Journal of Rock Mechanics and Mining Sciences,128,104238. https://doi.org/10.1016/j.ijrmms.2020.104238.

Hartlieb P, Toifl M, Kuchar F, Meisels R, Antretter T (2016) Thermo-physical properties of selected hard rocks and their relation to microwave-assisted comminution. Minerals Engineering,91,34-41,https://doi.org/10.1016/j.mineng.2015.11.008.

Saksala T (2021) Cracking of granitic rock by high frequency-high voltage-alternating current actuation of piezoelectric properties of quartz mineral: 3D numerical study. International Journal of Rock Mechanics and Mining Sciences. 147, 104891. https://doi.org/10.1016/j.ijrmms.2021.104891.